Simulation of microparticle inhalation in rhesus monkey airways

Taylor S. Geisler,[1,*] Madhu V. Majji,[1] Jana S. Kesavan,[2] Valerie J. Alstadt,[2] Eric S. G. Shaqfeh,[1,3,†] and Gianluca Iaccarino[3]

[1]*Department of Chemical Engineering, Stanford University, Stanford, California 94305-5025, USA*
[2]*US Army Edgewood Chemical Biological Center, Aberdeen Proving Ground, Maryland 21010-5424, USA*
[3]*Department of Mechanical Engineering, Stanford University, Stanford, California 94305-5025, USA*

(Received 9 June 2018; published 9 August 2019)

The flow in anatomically accurate rhesus macaque airways is studied using large eddy simulation. The deposition of inhaled 1- to 10-μm-diameter particles in the flow is also presented. The geometries comprise the nasal cavity, maxillary sinus cavities, pharynx, larynx, and trachea. Simulations are carried out for constant inspiratory flow rates of 2, 4, and 6 L/min, corresponding to Reynolds numbers of 351, 702, and 1053 for a nominal tracheal diameter of 0.8 cm. Unsteady flow is seen at certain flow rates, with the onset of turbulence occurring at constrictions in either the pharynx or glottis. The computed particle deposition results are compared extensively with experimental measurements carried out in models of the same computed tomography-based geometries, showing good agreement in the majority of cases. We observe significant deposition in the nasal airways as well as in the pharyngeal and laryngeal jet regions which dominate deposition for most particle sizes and flow rates. Inclusion of the pharynx and larynx regions of the upper airway in simulations is critical for accurately capturing the unsteady flow entering the lower airways, as well as predicting the fraction of inhaled particles that is filtered by the upper airways. Variability in airflow features, total particle deposition, and deposition locations between three monkeys is presented. These findings will allow better characterization of exposure dosages of inhaled compounds in animal experiments.

DOI: 10.1103/PhysRevFluids.4.083101

I. INTRODUCTION

The health effects of inhaled aerosols are often studied using nonhuman primate animal experiments and extrapolation of the results to humans [1]. In particular, rhesus macaque monkeys have been used in numerous inhalation dose-response toxicity studies as well as in pharmaceutical drug trials for inhaled medications [2–4]. Understanding the mechanisms governing the deposition of inhaled particles in rhesus monkeys is important for determining delivered dosages of inhaled compounds. Improved characterization of delivery dosages and locations are needed for translation to equivalent exposure scenarios in humans.

Inhalation toxicology studies have employed nonhuman primates due to the structural similarity to the human respiratory tract relative to other animal species [5,6]. Animal experiments using monkeys have been performed to quantify the effects of inhaled chlorine [7], ozone [8], formaldehyde [9], coal dust and diesel exhaust [10], manganese and lead particles [11,12], as well as infectious biologic agents [13,14]. Macaque monkeys (typically rhesus or cynomolgus) are the most commonly used nonhuman primates in such studies [3].

*tgeisler@stanford.edu
†esgs@stanford.edu

During typical resting breathing the majority of airflow is inhaled through the nasal passages and they are therefore the primary entryway for inhaled particles [2]. Several experimental studies have explored particle deposition in rhesus nasal airways. Kelly *et al.* measured the deposition of 1–10 μm diameter particles in an adult nasal replica cast over a range of inhalation flow rates [15]. Yeh *et al.* measured nanoparticle (5–200 nm) deposition using a nasal airway replica cast and also performed an *in vivo* study, reporting substantial nasal deposition [16,17].

In silico computational fluid dynamics (CFD) studies in idealized and realistic geometries have contributed much to the knowledge about inhalation and particle transport in lungs, as reviewed in several works [18–24]. CFD is ideal for studying turbulent fluctuations in airways as they are extremely difficult to measure in both *in vivo* and *in vitro* settings. These simulations also have the advantage of providing detailed information regarding the local deposition of particles. Using CFD, Kepler *et al.* reported vortical, laminar flow in the complex passages of the nasal airway of an adult rhesus monkey and simulated uptake of inhaled gases [25]. To our knowledge, only a single study exists, by Schroeter *et al.*, exploring the deposition of inhaled microparticles in the upper respiratory tract of monkeys using CFD [2]. They employ the same geometry as Kepler, along with an infant monkey geometry, and compute nanoparticle and microparticle deposition in the nasal airway during steady inhalation over a range of flow rates. Neither of these studies include the larynx or trachea of an adult rhesus monkey, and thus cannot capture the flow unsteadiness or deposition due to the pharyngeal and laryngeal jets. Schroeter *et al.* study an upper airway that includes the larynx and part of the trachea of an infant rhesus monkey, but did not provide details of the airflow or report any unsteadiness [2]. The present study includes these regions of an adult rhesus monkey.

Broadly speaking, the fate of inhaled particles is determined by the interplay of several factors including their physical and chemical properties, the breathing maneuver, and the details of the airway geometry. In addition, flow unsteadiness can widen regions of deposition of inertial particles compared to a steady flow via mixing and dynamic effects. Therefore, identifying the existence and intensity of flow unsteadiness is a significant consideration in the context of delivery of particles to the lower airways.

Recent advances in computed tomography (CT) technology allow the reconstruction of airway models with a high degree of geometrical detail [24,26–31]. CT-based geometries are currently limited in accuracy to a resolution of about 0.5 mm, which allows the reconstruction of airways which are several millimeters in diameter. The previously mentioned studies have considered geometries derived from CT or magnetic resonance imaging (MRI) scans. These studies have also considered a fixed flow rate under the assumption of quasi-steady-state behavior, which has been shown to be a good approximation for a range of breathing frequencies, particularly near the peak of the inspiratory or expiratory waveform [32].

Because of the complexity of the geometry, it is not straightforward to predict whether the flow that develops at a given flow rate will be steady or unsteady. Several CFD studies have examined the unsteadiness that develops in the larynx of humans using Reynolds-averaged Navier-Stokes (RANS) simulations in an idealized geometry [33] and in a cast-based geometry [34], as well as large eddy simulation (LES) in a CT-based geometry [27,28,34,35]. These researchers have noted that the turbulence generated in the upper airways can significantly effect the flow field and particle deposition patterns in the trachea and bronchial tree. By examining the distribution of turbulent kinetic energy they show that unsteadiness persists deeper into the lungs when the glottal constriction [34] and mouth-throat geometry [27,28,33] are included in the model. It is unknown as to whether a similar flow behavior exists in the airways of rhesus monkeys.

Motivated by the observations discussed above, one aim of the present study is to characterize the flow unsteadiness in rhesus monkey airways during inhalation. In particular, we examine the flow physics of the jet region in the upper airways. We also compute deposition of inhaled particles between 1–10 μm in diameter and examine the impact of individual geometric features on particle transport. We validate our particle deposition results with experiments performed in cast airways of the same geometries.

TABLE I. Genders, ages, and weights of the three rhesus monkeys used in airway generation.

	Gender	Age (years)	Weight (kg)
Monkey 1	Female	2	4.7
Monkey 2	Female	9	7.1
Monkey 3	Female	3	4.8

The problem formulation is given in Sec. II, including a description of the geometry and the numerical methodology. We then present our results in Sec. III. We analyze flow behavior and discuss particle transport and deposition, including a validation of the microparticle deposition predictions with experiments conducted in the same geometry and at the same flow conditions. Finally, we discuss our conclusions and the implications of our results in Sec. IV.

II. PROBLEM DESCRIPTION

A. Geometry

Three airway models are used, and are based on reconstructions from high-resolution CT scans, courtesy of researchers at the Department of Homeland Security's National Biodefense Analysis and Countermeasures Center (NBACC). The scans were taken of healthy female rhesus macaque monkeys of various ages and weights (Table I) in the supine position. Airway reconstruction was performed using the ITK–SNAP software. The reconstructed geometries comprise the nasal cavity, maxillary sinus cavities, pharynx, larynx, and trachea. The anatomical section of the model extends from the nostril inlets to a point near the end of the trachea preceding the main bronchi which serves as the outlet. Each model has closed lips and all flow enters through the nostrils. The *in silico* model additionally includes a flow conditioning cone section meant to reproduce inhalation from an ambient environment [Figs. 1(c) and 1(d)]. The rest of the model is congruent with the experimental geometry and includes the upper airways and trachea. The physical models used in the experiments were fabricated via stereolithography. The model airways were printed using an SLA Viper stereolithography machine and Somos WaterShed XC 11122 resin material.

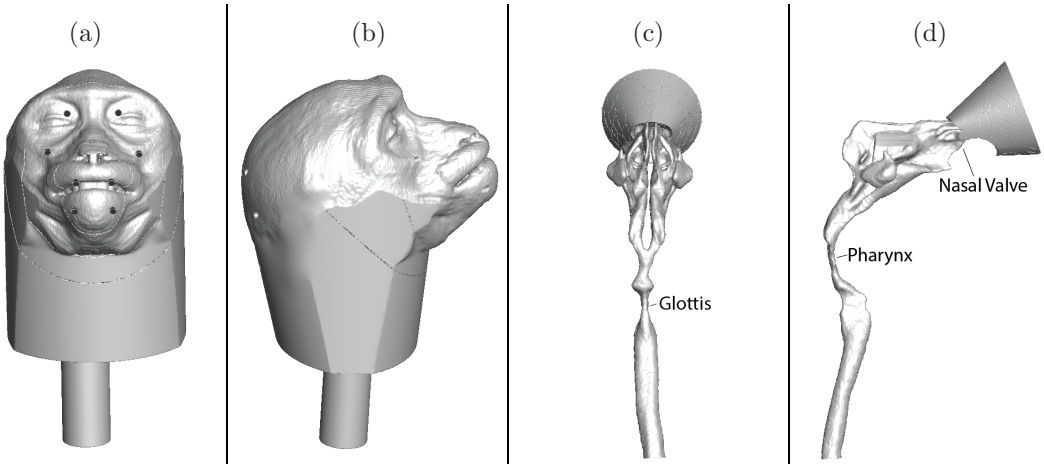

FIG. 1. Views of a 3D printed, CT-based geometry of Monkey 1 from the (a) front and (b) side and views of the numerical airway model from the (c) back, and (d) side, which includes a flow conditioning section.

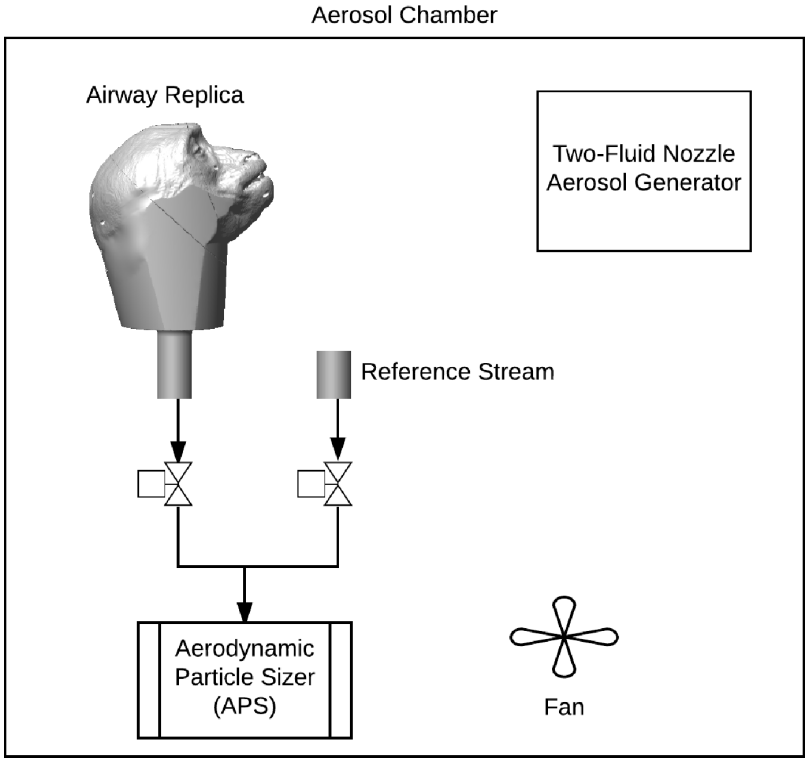

FIG. 2. Airway experiments were performed by placing the plastic airway replica into an aerosol chamber. Flow is driven through the airway and particle concentration at the airway outlet is recorded by an aerodynamic particle sizer.

B. Experimental methods

Microparticle deposition experiments using 3D printed plastic models of airway geometries are performed for comparison to the CFD simulations detailed here. Airway models are placed into a large plexiglass aerosol chamber (with dimensions of 1.52 × 0.91 × 1.22 m) and a pump is attached to the airway outlet to simulate inhalation at each flow rate. Polydisperse Arizona road dust (ARD) particles are suspended in the aerosol chamber using an aerosol generator from which air is drawn into the plastic airway model. An aerodynamic particle sizer (APS) positioned at the airway outlet measures the concentration of ARD particles with aerodynamic diameters in the range of 0.5–11 μm. The air-particle suspension is drawn into the nostrils and through the hollow airway model to simulate inhalation. The air-particle suspension exiting the trachea is routed directly to an APS for measurement of particle concentrations for a range of particle sizes. A second air-particle stream is also sampled from the chamber that leads directly to another APS as a reference. The two sampling streams are located in close proximity to each other in the chamber to achieve equivalent inlet particle concentrations, and a mixing fan is placed in the airway chamber to homogenize the particle suspension. Air in the chamber was mixed for 45 s via a fan after the introduction of ARD. A solenoid switch enabled the operator to switch APS sampling between streams. Lines and fittings were identical for the upstream and downstream sides and were carefully constructed to minimize losses in the airflow path. The reported experimental particle deposition fraction is calculated by comparing particle concentrations of the reference stream and the stream that exits the airway. The experimental setup is illustrated in Fig. 2.

Before each experimental run, air with a small amount of nebulized corn-oil droplets is briefly flowed through the airway to create an adsorptive airway surface. During each run the air-ARD suspension is flowed through the airway and 10 measurements of particle concentration are made for both the airway exit and reference streams. Three runs were performed at each flow rate and each measurement is averaged over 20 s of inhalation. Average deposition fractions are reported. Inspiratory flow rates of 2, 4, and 6 L/min of air are tested. These correspond to relevant psychological breathing conditions as reported in the review by Asgharian *et al.* [36] and may roughly be considered as conditions of resting, light activity, and heavy activity respectively.

C. Numerical method and simulation set-up

The simulations were performed using CDP, an incompressible Navier-Stokes (NS) solver developed at Stanford's Center for Turbulence Research to perform LES in complex geometries. CDP has been extensively documented elsewhere [37,38]. Briefly, the NS equations are discretized using a node-based finite volume formulation for arbitrary unstructured meshes. Time advancement of the linear terms in the momentum equations uses the semi-implicit Crank-Nicholson scheme, while the nonlinear terms are discretized using a combination of the Crank-Nicholson and Adams-Bashforth schemes. The algorithm follows a fractional step method that ensures a divergence-free velocity field. An estimation of the Kolmogorov length scale with an integral scale of 0.8 cm and at the Reynolds numbers of 351, 702, and 1053 yields η of 99, 59, and 43 μm respectively [39], which are all less than an order of magnitude smaller than the bulk resolution of 250 μm. The Kolmogorov timescales at Re 351, 702, and 1053 are, respectively, 0.64, 0.23, and 0.12 ms. The unresolved scales are modeled using the dynamic Smagorinsky subgrid scale (SGS) model, which estimates locally the eddy viscosity as a function of time and space. The resulting subgrid-scale stresses vanish in laminar flow and at solid boundaries [40]. CDP has been validated in simulating turbulent flow in a realistic human lung in a prior study at Stanford [35].

A uniform velocity Dirichlet boundary condition is applied at the inlet of the flow conditioning section to obtain constant inspiratory flow rates of 2, 4, and 6 L/min of air. This corresponds to Reynolds numbers of 351, 702, and 1053 for a nominal tracheal diameter of 0.8 cm. The density and kinematic viscosity of the air are $\rho^f = 1.205$ kg/m^3 and $\nu = 1.51 \times 10^{-5}$ m^2/s. A no-slip boundary condition is applied along the rigid walls. A convective outlet boundary condition is enforced at the trachea exit.

To ensure development of the flow before gathering statistics and injecting particles, the velocity and pressure were monitored at probes located throughout the anatomical section. The simulation was run with a constant Courant-Friedrichs-Lewy (CFL) number of 1.0. Flow statistics were averaged over 2 s, resulting in statistically stationary velocity and pressure fields.

Particles were treated as Lagrangian point particles and are injected uniformly over the flow inlet with the velocity of the local flow and density of $\rho^p = 1000$ kg/m^3. Particles are subject to a stokes drag force, a gravitational force, and a Brownian force. The trajectories of particles are calculated by solving the following equations:

$$\frac{d\bar{u}_i^p}{d\bar{t}} = \frac{\bar{u}_i^f - \bar{u}_i^p}{\mathrm{St}k} + \frac{\bar{g}_i}{\mathrm{Fr}^2}, \tag{1}$$

$$\frac{d\bar{x}_i^p}{d\bar{t}} = \bar{u}_i^p, \tag{2}$$

where superscript p denotes variables associated with particle and superscript f denotes variables associated with the fluid. The Stokes number relating particle relaxation time due to drag to a characteristic flow time is

$$\mathrm{St}k = \frac{\tau U_c}{L_c}. \tag{3}$$

The particle relaxation time is

$$\tau = \frac{\rho^p d^2}{18\mu}[1 + 0.15(\mathrm{Re}^p)^{0.687}]^{-1}, \tag{4}$$

where Re^p is the particle Reynolds number given by

$$\mathrm{Re}^p = \frac{\rho^f d U_c}{\mu}\left|\bar{u}_i^p - \bar{u}_i^f\right|. \tag{5}$$

All plots showing deposition as a function of stokes number take Re^P as zero in the Stokes number calculation. The Froude number, which relates the relative effects of advective transport and gravitational settling, is

$$\mathrm{Fr} = \frac{U_c}{\sqrt{g_c L_c}}, \tag{6}$$

with a characteristic gravity term given by

$$g_c = g\frac{\rho^p - \rho^f}{\rho^p}. \tag{7}$$

In the equations above, $\bar{u}_i$, $\bar{x}_i^p$, ρ, μ, d, and g denote dimensionless velocity, dimensionless particle position, density, viscosity, particle diameter, and gravitational acceleration, respectively. U_c and L_c are the characteristic velocity and length scale of the flow. A Brownian motion term is added at the end of each particle time step:

$$\bar{x}_i^p += \frac{\sqrt{2Ddt}}{L_c}\mathcal{N}_i(0, 1), \tag{8}$$

where D is the diffusion coefficient of the particle given by kinetic theory

$$D = \frac{k_B T}{3\pi\mu d}, \tag{9}$$

dt is the simulation time step, $\mathcal{N}_i(0, 1)$ is a three-dimensional Gaussian random variable with mean 0 and variance 1 in each of the three cardinal directions, T is the temperature (37 °C), and k_B is the Boltzman constant. The Peclet number quantifies the ratio of advective transport to diffusive transport:

$$\mathrm{Pe} = \frac{dU_c}{D}. \tag{10}$$

Particle trajectories are integrated using a Runge-Kutta 3 integration scheme with a particle time step equal to 0.01 of the particle relaxation time. Microparticle transport in airways is commonly modeled as a two-phase flow problem, assuming dilute particle suspensions in light of the low experimental particle volume fractions ($<10^{-7}$) and employing an Euler-Lagrange approach [41]. Thus, we assume diluteness and use one-way momentum coupling where the Lagrangian particles do not affect the background flow. The particles do not interact with one another. A particle is considered deposited when its center is less than a particle radius from any wall. Simulations terminate when every particle exits from the outlet or is deposited along the airway wall. The simulations were conducted on 480 CPU cores of the U.S. Air Force's Lightning cluster.

D. Mesh-independence analysis

Hybrid meshes with tetrahedral elements in the bulk and multi-layered prismatic wall elements are used. The maximum mesh size throughout the bulk of the domain is approximately 0.25 mm, and this also corresponds to the maximum tangential resolution at the walls. Eight mesh layers, each

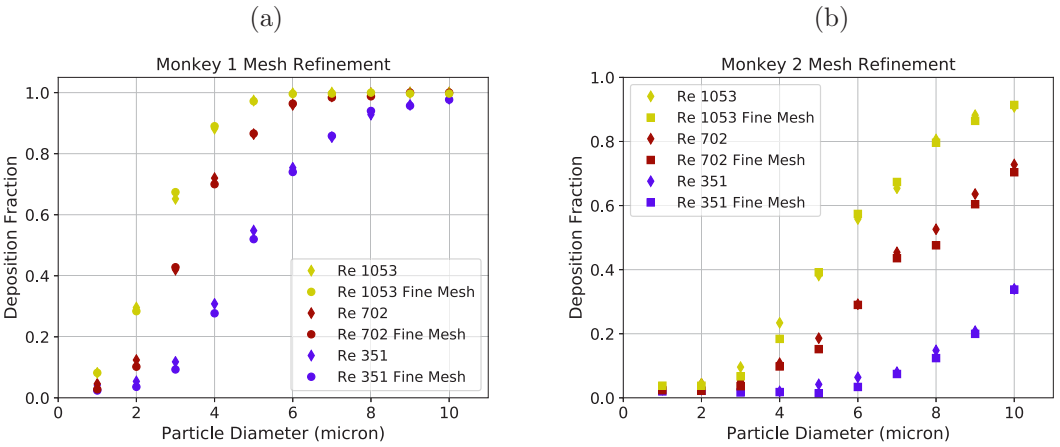

FIG. 3. Mesh refinement produces small (<0.05) changes to particle deposition fraction in (a) Monkey 1 and (b) Monkey 2 when increasing mesh size from 4 to 13 million control volumes at all flow rates and particle sizes.

with with a thickness of approximately 0.05 mm, were created to resolve wall gradients. Meshes contain approximately 4 million control volumes.

A mesh refinement study was performed to ensure convergence of particle deposition results. Simulations were performed for Monkeys 1 and 2 on meshes containing roughly 13 million control volumes. These meshes have a maximum resolution of 0.1 mm in the bulk and eight layers along the boundaries, each with with a thickness of 0.03 mm. Total particle deposition fractions changed by less than 0.02 on average with refinement, and the maximum change was 0.05 (Fig. 3).

To verify the accuracy of the LES model for capturing subgrid scale stresses, a refined mesh was created at the Kolmogorov length scale to perform direct numerical simulation (DNS) of the unsteady flow. This mesh has a maximum scale of 0.1 mm in the bulk and 59 μm (the estimated Kolmogorov length scale at Re 702) in the region from the larynx to mid-trachea where the development of turbulence is observed. The DNS mesh contains 51 million control volumes.

III. RESULTS

A. Flow

The results of flow simulations are presented on slices throughout the geometry and an analysis of relevant flow features is performed. Flow velocities are made dimensionless with the nominal (0.8 cm diameter) mean tracheal flow velocity at Re 351, or 0.663 m/s. The slices have been arranged such that flow is into the page. The nasal airway consists of nearly symmetric left and right passages separated by a planar septum. Flow is therefore only visualized through the right nasal passage. Coronal slices are taken from the nasal vestibule to the posterior nasal cavity and are shown in Fig. 4. Slices are taken at roughly equivalent positions in all monkeys. The degree of geometric variation between monkeys is apparent from these visualizations.

Laminar flow is observed throughout the nasal passage at all flow rates and for all monkeys. The highest flow velocities in the nasal cavity are observed in the narrow nasal valve in the anterior airway near the second slice of Fig. 4. This high-velocity stream of air passes into the main nasal cavity and subsequently impinges on the margin of the middle turbinate. Airflow proceeds through the narrow meatuses surrounding the turbinates. Significant variability is seen in the shape of the inferior and superior dorsal streams between monkeys. Most notably, Monkey 3 completely lacks an inferior dorsal stream. Additionally, maxillary sinus volumes vary drastically between individual monkeys. Low velocity flow is observed in the maxillary sinus cavities.

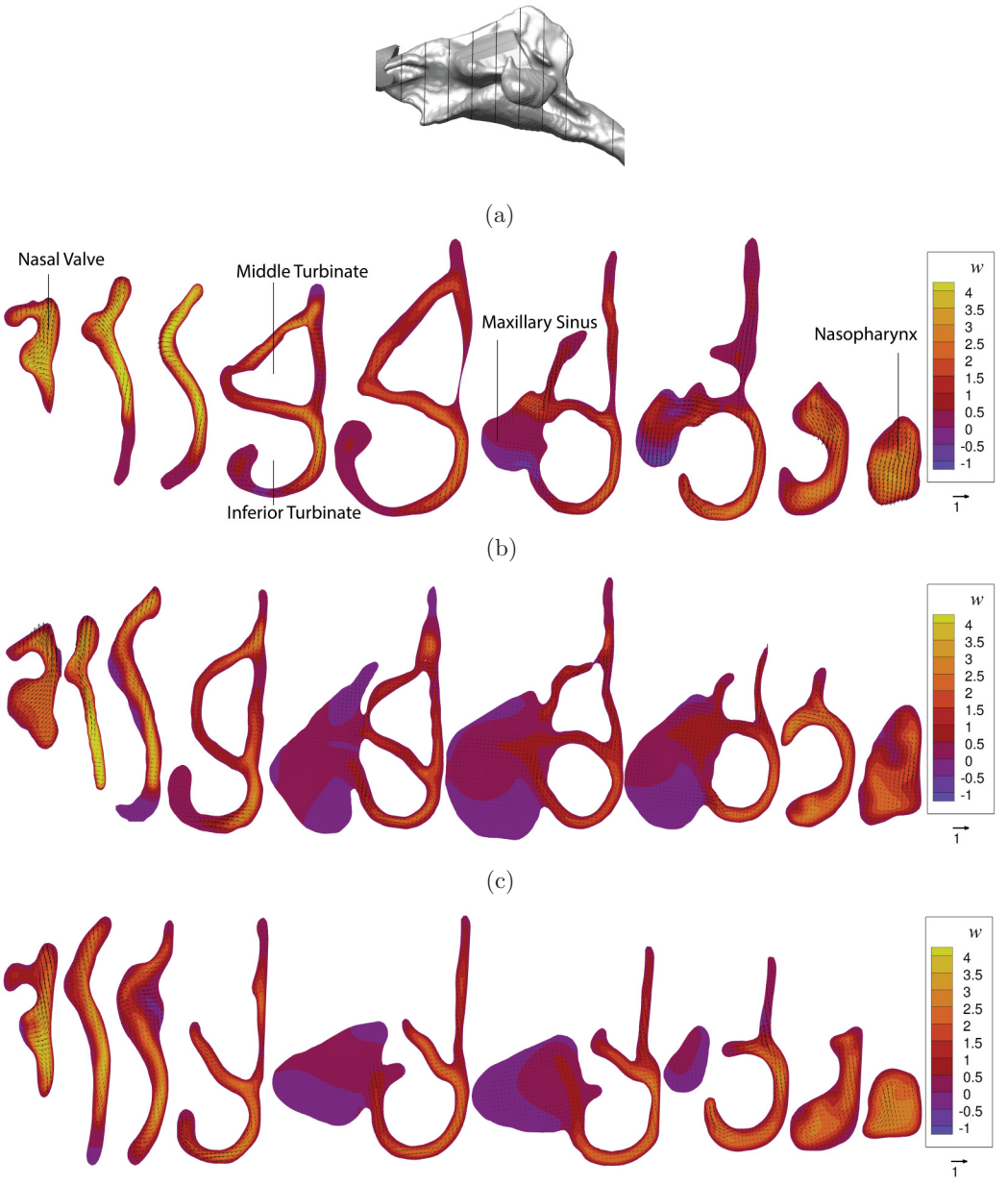

FIG. 4. Comparison between right nasal airflow in (a, below panel label) Monkey 1, (b) Monkey 2, and (c) Monkey 3 at Re 702. The contour variable w corresponds to the streamwise velocity normal to the slice while the superimposed vectors correspond to the in-plane velocity.

The geometry of the pharynx and larynx are complex and significantly impact the flow entering the trachea. Figure 5 shows the time-averaged velocity fields on slices in this region. The airways severely constrict in the pharynx, shown in the first slice of Fig. 5. The minimum cross-sectional area varies drastically between individuals here, and is more than five times larger in Monkey 3 than Monkey 1 (Table II). The airway following the pharynx rapidly expands, and a high-velocity pharyngeal jet can be distinguished in the second slice of Fig. 5. The flow velocity of the jet is

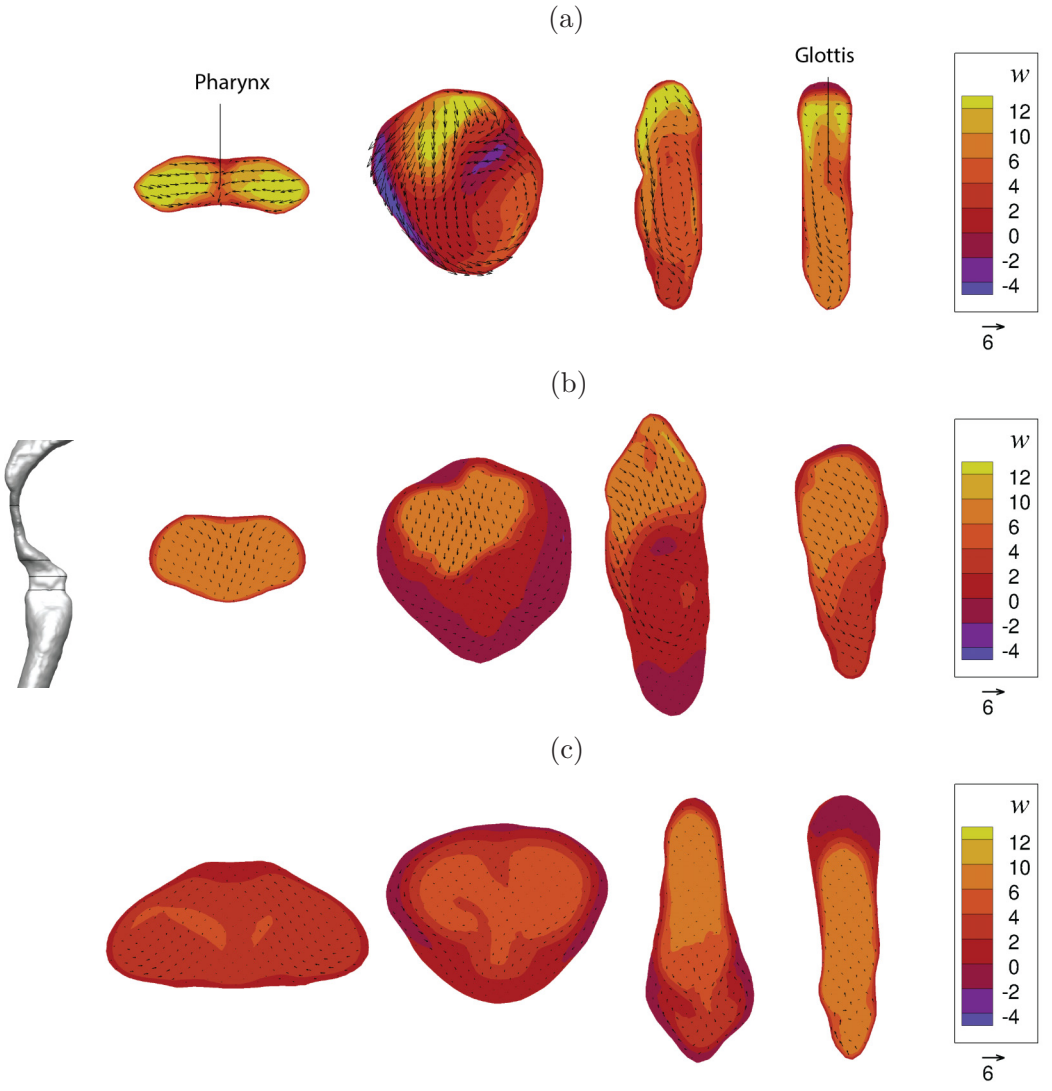

FIG. 5. Comparison between airflow in the pharynx and glottis in (a) Monkey 1, (b) Monkey 2, and (c) Monkey 3 at Re 702. The contour variable w corresponds to the mean streamwise velocity normal to the slice while the superimposed vectors correspond to the mean in-plane velocity.

TABLE II. Cross-sectional areas in cm^2, hydraulic diameters (D_H) in cm, and Reynolds numbers ($Re = QD_H/A\nu$) at the narrowest point in the nasal airway, pharynx, and glottis at a nominal tracheal Re of 702.

	Nasal Valve:	Area	D_H	Re	Pharynx:	Area	D_H	Re	Glottis:	Area	D_H	Re
Monkey 1		0.462	0.54	518		0.058	0.17	1312		0.136	0.33	1062
Monkey 2		0.413	0.51	548		0.138	0.37	1192		0.207	0.44	933
Monkey 3		0.579	0.61	462		0.320	0.55	754		0.160	0.36	989

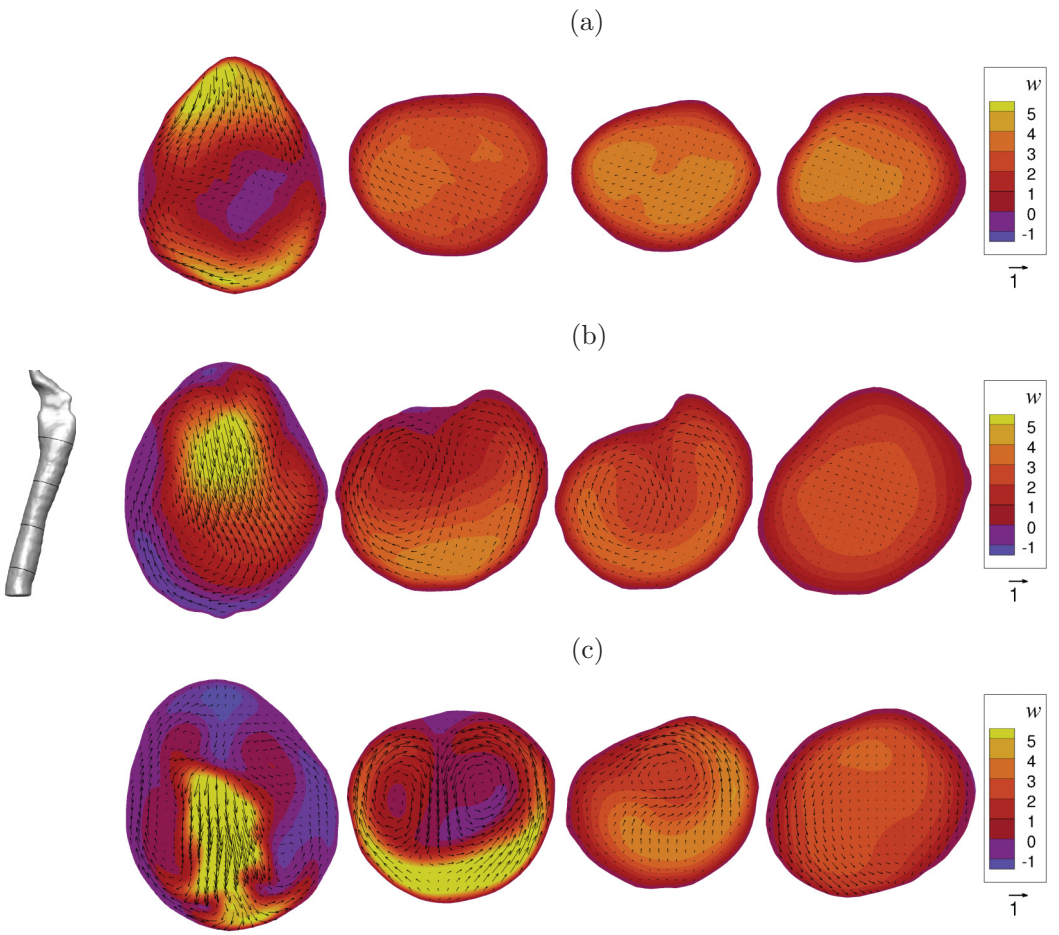

FIG. 6. Comparison between airflow in the trachea in (a) Monkey 1, (b) Monkey 2, and (c) Monkey 3 at Re 702. The contour variable w corresponds to the mean streamwise velocity normal to the slice while the superimposed vectors correspond to the mean in-plane velocity.

highest in Monkey 1 due to the highly-constricted pharynx. Flow inertia favors the bias of the jet toward the posterior airway. A notable feature is the region of flow separation and recirculation in Monkey 1. Secondary flow toward the front of the monkey, shown as in-plane vectors, is due to the airway curvature forcing the flow to turn.

An analogous constriction feature is also seen in the glottis and produces the characteristic laryngeal jet as the airway expands into the trachea. The long axis of the glottal constriction is roughly perpendicular to that of the pharynx. This constriction is shown in the fourth slice of Fig. 5. Time-averaged velocity fields for slices in the trachea are shown in Fig. 6. Recirculation regions form in the upper trachea, but their locations vary between individuals. Monkey 1 has recirculation in the center of the trachea, Monkey 2 the anterior, and Monkey 3 the posterior [Slice 1 of Fig. 6]. These separation regions inject momentum into the in-plane flow, generating counter-rotating vortices in Monkeys 2 and 3. The secondary flow structures decay throughout the trachea as the flow develops.

The regions of flow separation and adverse pressure gradients in rapidly expanding regions following the geometric constrictions of the pharynx and glottis produce turbulent flow at some flow rates. This unsteadiness is observed at Re 702 and 1053, except in Monkey 1 which develops

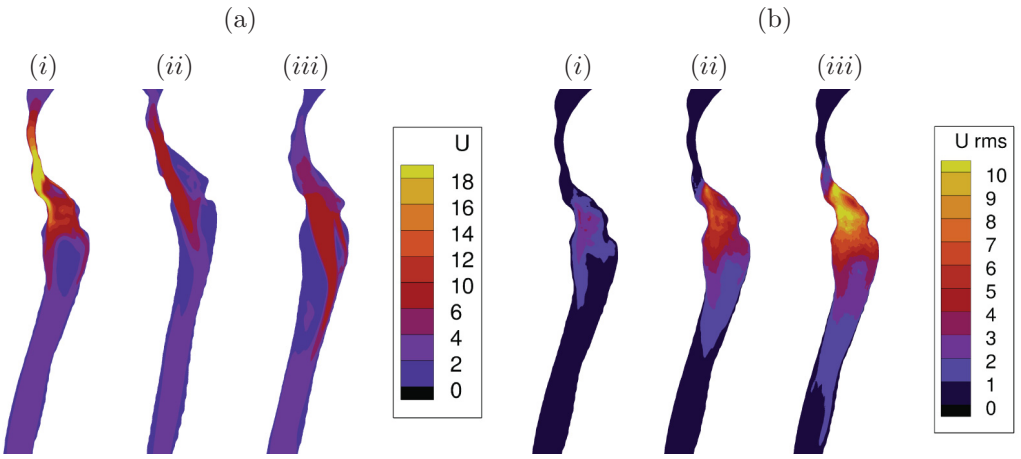

FIG. 7. (a) Magnitude of the mean flow velocity at nominal tracheal Re of 702 for (i) Monkey 1, (ii) Monkey 2, and (iii) Monkey 3. A high-velocity laryngeal jet forms in the narrow constrictions of the pharynx and glottis. (b) Magnitude of the root mean square of flow velocity reveals turbulence generation in the larynx of Monkey 1 at (i) Re 351, (ii) Re 702, and (iii) Re 1053.

turbulent flow at all flow rates. Maximal flow unsteadiness is observed in the larynx and upper trachea, and the magnitude of velocity fluctuations increases with Re [Fig. 7(b)]. Unsteadiness of the velocity signal decays throughout the trachea. Turbulence is triggered in the pharynx in Monkeys 1 and 2, but not until the glottis in Monkey 3 due to its lower pharyngeal Re (Table II).

DNS of turbulence is free of the modeling assumptions implied by the SGS closure and is therefore useful for validation of LES results. DNS has previously been performed in the human upper airways by Wang and Elghobashi [42], but to our knowledge has never been used to study the rhesus monkey upper airways. We performed DNS in Monkey 2 at Re 351 and Re 702 for particle sizes from 8–10 μm using the DNS mesh described previously. Results were compared to the three-dimensional flow fields and particle deposition predictions of LES. In the Re 351 case at this finer mesh density, steady laminar flow was observed consistent with the LES prediction. For the Re 702 case the flow and pressure fields are virtually indistinguishable for the two models as expected in the laminar flow of the nasal passage regions where the adaptive SGS stress term in the LES model reduces to zero. The orientation of the laryngeal jet in the upper trachea is seen to angle slightly more toward the front of the trachea in the DNS model as shown in Fig. 8. DNS also predicts a slightly later development of flow unsteadiness after the larynx but mean velocity fluctuation magnitudes are within 5% of LES at each slice in the trachea where both models show unsteadiness. Despite these differences, the fraction of particles deposited changed by less than 3% for every Reynolds number and particle size tested as shown in Fig. 9(b). We conclude that LES is accurately predicting the quantities of interest to within a few percent of DNS simulations at significantly lower computational cost.

B. Particles

1. Validation of total deposition

Comparison of *in silico* predictions of particle deposition to *in vitro* tests is a way to evaluate the accuracy of our modeling results. This section contains a comparison of the simulation predictions of deposition fraction (DF) to measurements obtained via model airway experiments. The DF is defined as the ratio of the number of particles deposited to the number that enter at the inlet. Figure 9 shows experimental results and simulation results based on the present LES model. These plots

	LES	DNS	
Slice	$\bar{U}_{RMS}/U_T$		Δ (%)
1	1.34	0.56	-58
2	1.63	0.96	-41
3	1.90	1.83	-4
4	1.14	1.10	-4
5	0.74	0.76	3

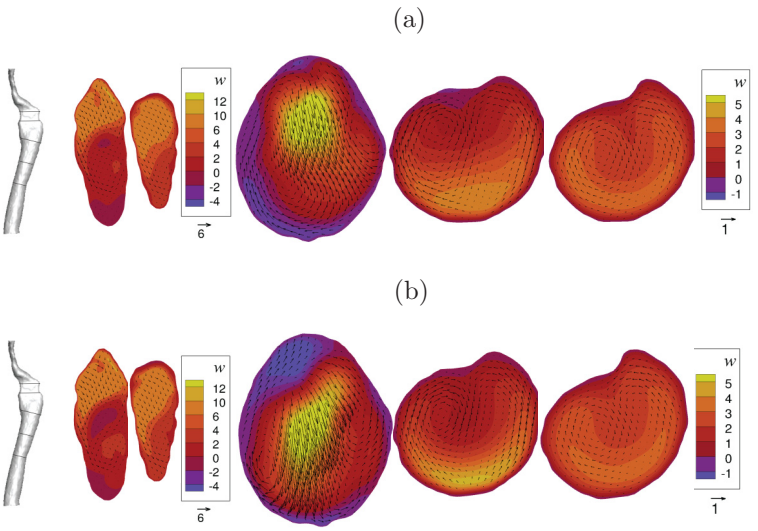

FIG. 8. Comparison between (a) LES and (b) DNS results in the larynx and trachea of Monkey 2 at Re 702. The contour variable w corresponds to the mean streamwise velocity normal to the slice while the superimposed vectors correspond to the mean in-plane velocity. The parameter shown in the table is the dimensionless average root-mean-square of the velocity ($\bar{U}_{\mathrm{RMS}}/U_T$) for each slice made dimensionless with the nominal mean tracheal flow velocity (U_T) at Re 351, or 0.663 m/s. The percentage change between LES and DNS is shown as Δ. Slices are numbered from left to right.

show DF as a function of particle diameter at each Reynolds number. Deposition was computed for particles with diameters in the range of 1–10 μm at 3 Reynolds numbers and for three monkeys, for a total of nine study cases.

Agreement with experimental deposition measurements in Monkey 1 is excellent for all Reynolds numbers and particle sizes. The computational data points in Fig. 9(a) clearly retrace the curves of measured deposition data. The average difference in DF between experiment and simulation for all 30 data points in Monkey 1 is 2.4%. DF increases to near-unity for all Reynolds numbers at a particle diameter of 10 μm in both experiment and simulation. Agreement with experiment is good at the Re 702 and 1053 cases in Monkey 2, shown in Fig. 9(b). The average deviation from those measurements is 4.8%. Agreement in the Re 702 and 1053 cases in Monkey 3 is worse with an average difference of 8.4% [Fig. 9(c)].

Disagreements in particle deposition efficiency between experiment and simulation can be partially attributed to differences in geometry and potential unmodeled effects in simulations. In particular, the largest discrepancies appear in the laminar flow cases near the critical Re of transition to turbulent flow in the pharynx/larynx region (the Re 351 cases in Monkeys 2 and 3 have average DF differences of 11.0% and 16.1% relative to experimental measurements). Because total DF is low for those cases predictions of simulations and experiments are 1–2 times different for Monkey 2, and 2–3 times for Monkey 3. Flow in the laboratory setting is potentially turbulent there, which would suggest the presence of an unmodeled forcing such as a pump vibration or surface roughness due to the model printing process. This could explain the poor agreement in the laminar Re 351 cases, as deposition is expected to be highly sensitive over a laminar-to-turbulent flow transition. Other factors that are neglected in the simulations and may contribute to differences in predicted deposition include particle shape factors and more complex particle-wall interactions.

These comparisons instill ample confidence in the applicability and accuracy of the present LES particle deposition results.

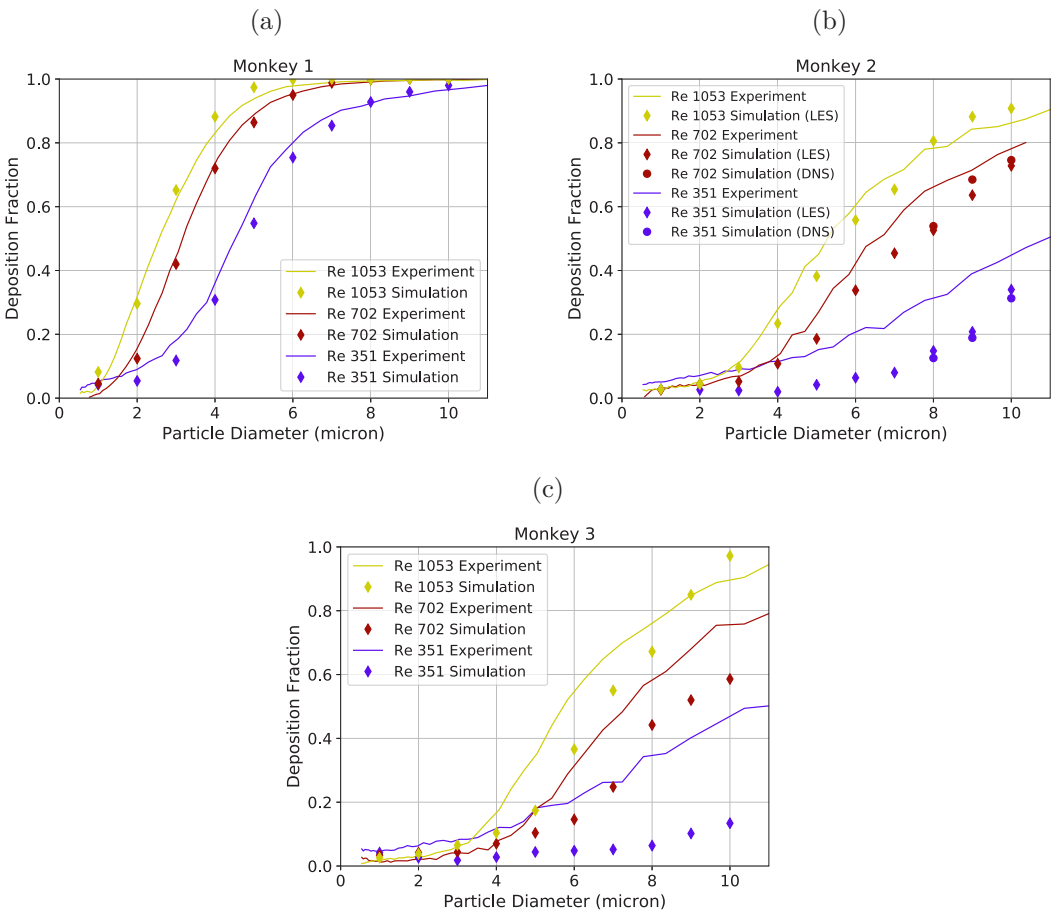

FIG. 9. Total deposition fraction predicted by simulations compared with experimental measurements in (a) Monkey 1, (b) Monkey 2, and (c) Monkey 3.

2. Analysis

This section contains an analysis of the simulation predictions of total DF as well as deposition patterns. Computed DF results are shown in Fig. 9 as diamond symbols and show monotonic increase with particle diameter in every case. In Monkey 1 microparticle DF displays sigmoidal behavior, with efficiencies of a few percent or less at 1 μm and 100% for 10 μm particles at Re 702 and 1053. Total deposition is less in Monkeys 2 and 3 and increases more gradually with particle size than in Monkey 1. DF is below 100% for even the largest tested particle size in Monkeys 2 and 3.

Particle deposition will be considered in two general regions of the airway, the nasal airways and the larynx/trachea. Deposition in the larynx/trachea is larger than in the nasal airways at all but the highest Reynolds number and particle sizes in Monkeys 1 and 2 (Fig. 10). Nasal DF of 10 μm particles at the Re 1053 case is 55, 59, and 40% for Monkeys 1, 2, and 3 respectively. This result is in contrast to previous studies that found that rhesus nasal airway DF reached unity for particles on the order of 10 μm at similar flow rates [2]. At Re 1053 deposition in the larynx/trachea declines at the largest particle sizes due to upstream filtering of particles in the nasal airway for all monkeys. It can be seen that both nasal and laryngeal/tracheal deposition effects are considerable in the context of microparticle inhalation in rhesus monkey airways.

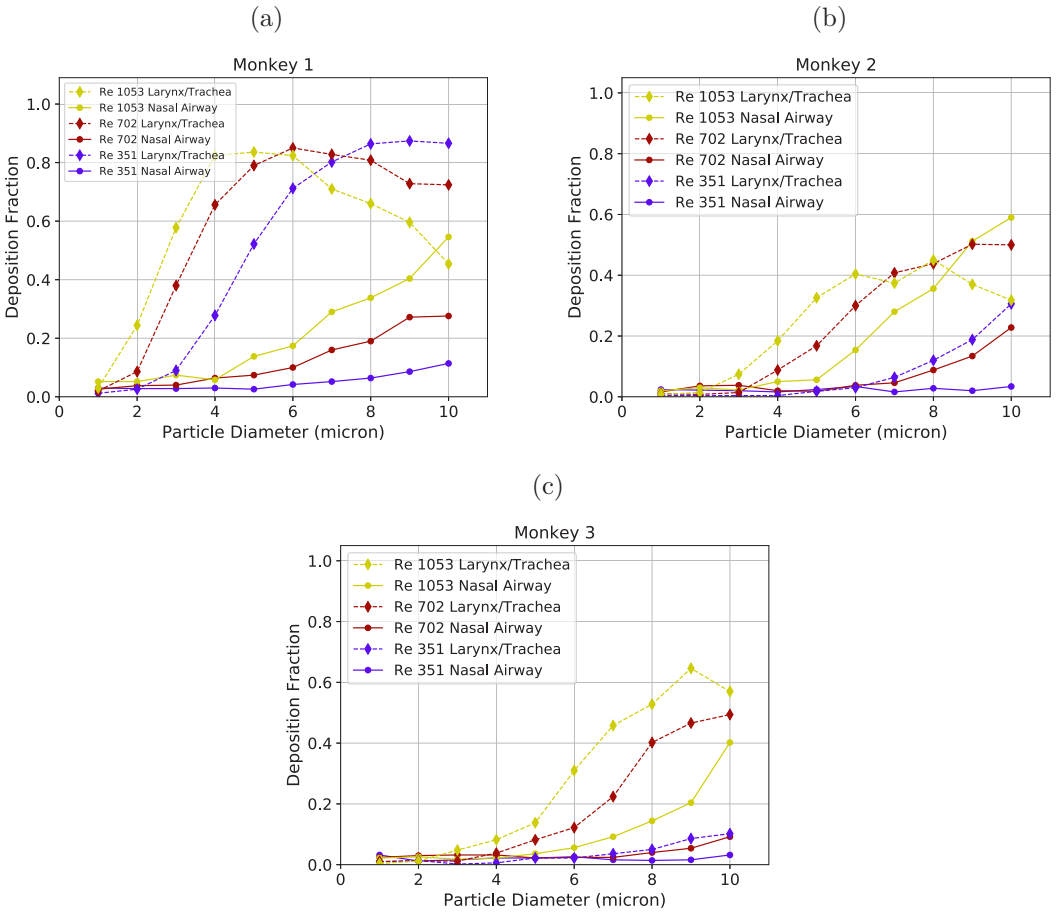

FIG. 10. Nasal airway and trachea/larynx deposition fractions predicted by simulations in (a) Monkey 1, (b) Monkey 2, and (c) Monkey 3.

Figures 11 and 12 show the deposition of 6 and 10 μm particles in the nasal airways and larynx/trachea of each monkey at Re 702. The figures show deposition locations of 10 000 injected particles at each size to demonstrate local deposition patterns in each monkey. Deposition in the nasal passages occurs at three major hot spots, i.e., the nasal valve region, the front and top of the middle turbinate, and the walls of the descending nasopharynx. All deposition hot spots share the characteristic of abrupt geometric changes. Particles deposit in the nasal valve region due to the constriction of the airway there. This is particularly apparent for 10 μm particles in Monkeys 1 and 2 which have the most constricted nasal valves, but some deposition is seen here for all monkeys. Significant deposition also occurs at the point of impingement of the high-velocity nasal valve stream onto the middle turbinate. At this feature streamlines curve around the turbinate and into the surrounding meatuses. At larger particle diameters and flow rates, significant deposition is additionally seen in the posterior superior wall of the nasal cavity as the superior dorsal stream descends at the nasopharynx, causing curved streamlines and a mechanism for inertial impaction. Nasal deposition is most disperse in Monkey 3 as fewer particles are deposited in the nasal valve entrance region. Enhanced deposition in the lower nasal airway is due to Monkey 3 lacking the meatus superior to the middle turbinate and biasing flow to the inferior nasal airway.

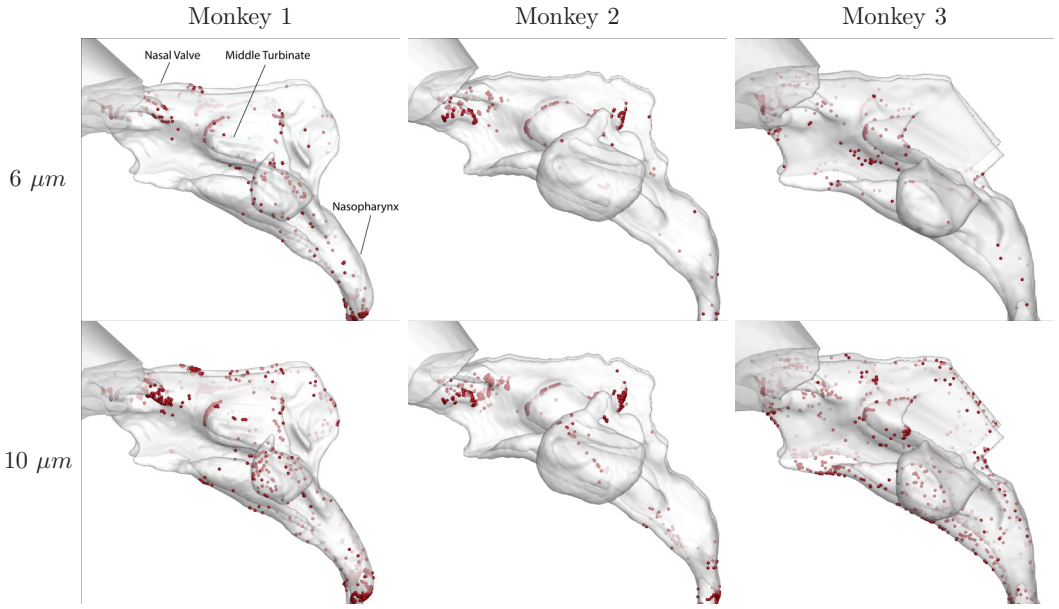

FIG. 11. Local deposition of 6 and 10 μm particles in the nasal passages at Re 702 show deposition hot spots in the nasal valve region, the top of the middle turbinate, and the nasopharynx.

Local deposition in the larynx/trachea region is shown in Fig. 12. DF in this region is larger in Monkey 1 than Monkeys 2 and 3. This is explained by the higher velocity pharyngeal jet that forms in Monkey 1 and impinges on the posterior wall of the larynx [Fig. 7(a)]. The pharyngeal/laryngeal jets in Monkeys 2 and 3 have significantly lower velocities and do not impact the larynx wall

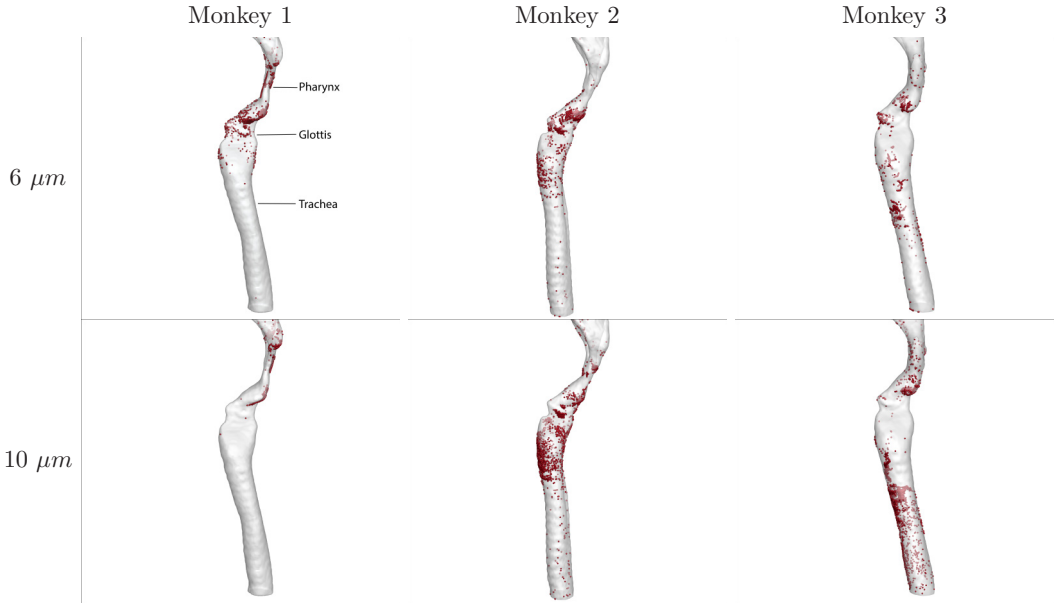

FIG. 12. Local deposition of 6 and 10 μm particles in the larynx and trachea at Re 702. Differences in the pharyngeal/laryngeal jet features produce significantly different deposition patterns between monkeys.

TABLE III. Dimensionless parameter ranges reinforce the finding that inertial effects dominate particle transport.

Case:	Stokes Number	Flow Rate (L/min)	Particle Diameter (μm)
Min Stokes Number	2.0×10^{-3}	2	1
Max Stokes Number	0.61	6	10
	Froude Number	Flow Rate (L/min)	Particle Diameter (μm)
Min Froude Number	13.4	2	1-10
Max Froude Number	40.2	6	1-10
	Peclet Number	Flow Rate (L/min)	Particle Diameter (μm)
Min Peclet Number	1.1×10^{5}	2	1
Max Peclet Number	3.3×10^{7}	6	10

directly [Figs. 5 and 7(a)] resulting in lower deposition in the larynx and enhanced deposition on the front wall of the trachea. These findings suggest that geometric differences in the pharynx/larynx double-constriction feature alter both the flow profile, as shown in the previous section, and aerosol deposition locations considerably.

The secondary flows (e.g., counter-rotating vortices in Monkeys 2 and 3) increase in strength with flow rate and also contribute to the preferential particle concentration along the margins of the airway and depletion of particles along the airway centerline (Fig. 6). These particle-free zones in the trachea will certainly have effects on downstream deposition sites. Unsteady flow broadens deposition regions of particles due to turbulent dispersion. Deposition along the side and back walls of the trachea in Monkeys 2 and 3 is due to turbulent dispersion and these secondary flows.

The observation that deposition occurs in different locations between different particle sizes and airway geometries implies that a simple stokes number collapse of particle deposition curves should not be expected. Rather, patient-specific deposition predictions may be required to accurately asses delivery of particles to the lower airways. Differences in the pharynx/larynx constriction features can produce widely different deposition patterns and fractions. Future studies should explore the time-dependent geometric changes expected in the pharynx/larynx geometry during the breathing cycle as a result of the revelations that the deposition is highly sensitive to changes in these features.

A test case with no Brownian motion yielded equivalent deposition results, demonstrating that the effect of these physics is small in the upper airways and trachea compared with inertial impaction,

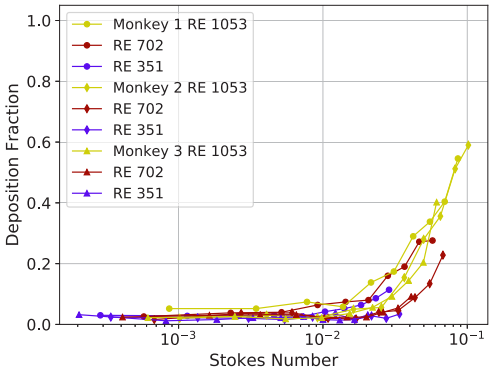

FIG. 13. Nasal airway deposition at all flow rates and monkeys when plotted by Stokes number. The characteristic length is defined as: $L_c = \sqrt{\frac{4A_{cs}}{\pi}}$ with A_{cs} being the minimum cross-sectional area at the nasal valve.

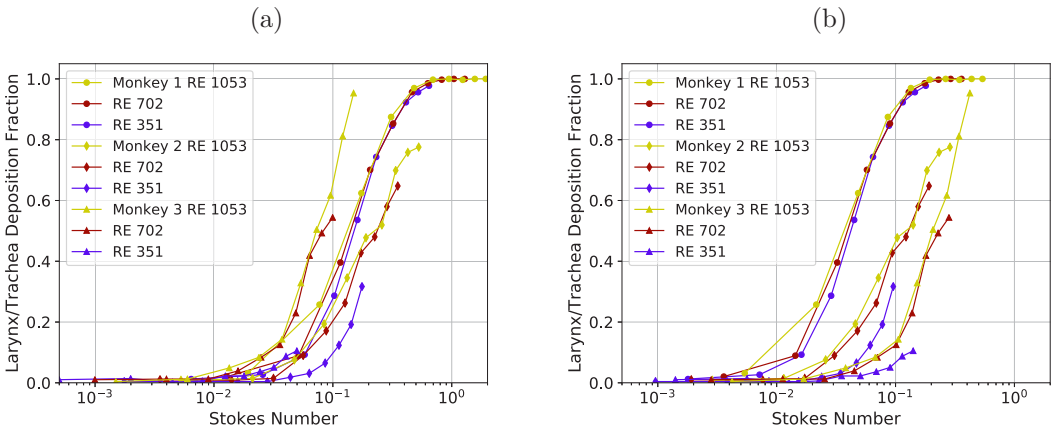

FIG. 14. Deposition fraction in the larynx and trachea at all flow rates and monkeys when plotted by Stokes number. The characteristic length is defined as: $L_c = \sqrt{\frac{4A_{cs}}{\pi}}$ with A_{cs} being the minimum cross sectional area at the (a) pharynx and (b) glottis.

gravitational settling, and turbulent dispersion. Using the nominal hydraulic diameter at the glottis as a characteristic length (L_c) and the mean velocity through this constriction as a characteristic velocity (U_c) the Peclet number ranges from 1.1×10^5 to 3.3×10^7 in these simulations, again suggesting that diffusive transport is many orders of magnitude smaller than convective transport effects (Table III). Particle Stokes numbers range from 8.1×10^{-6} to 2.4×10^{-2}, supporting the observation that inertial impaction is the leading mechanism of deposition. The minimum and maximum Froude numbers are 13.4 and 40.2, suggesting that the gravitational effect on particle transport is an order or magnitude smaller than convective transport, but is not entirely negligible.

The dominance of inertial effects on deposition in the nasal passages and trachea is well established in human airways, and we see this to be true in rhesus monkey airways as well. The collapse of adsorption to St is apparent in the nasal passage, as seen in Fig. 13 across monkeys and flow rates. A collapse of deposition curves in the larynx/trachea region is also seen, although it is worse than in the trachea due to significantly different deposition locations between monkeys and the transition from laminar to turbulent flow between flow cases in Monkeys 2 and 3 (Figs. 12 and 14). This gives insight into the magnitude of deposition variability between individual monkeys. The collapse is seen to be better when the characteristic length is defined using the cross section of the pharynx compared to the glottal cross section.

IV. CONCLUSIONS

In this work, we studied the flow and particle deposition throughout CT-based models of rhesus monkey airways that extend from the nasal cavity to the trachea exit. LES simulations at constant inspiratory flow rates of 2, 4, and 6 L/min of air, relevant to breathing conditions from low to high exertion and inhalation devices, were performed. This corresponds to tracheal Reynolds numbers of 351, 702, and 1053. We carried out a validation against particle deposition experiments in the same airway geometries. We observed good agreement with experimental data, capturing overall deposition fractions well in each airway at most flow rates. Laminar flow is observed in the nasal airways at all Reynolds numbers. We find that the flow becomes unsteady in the pharynx or glottis at some Reynolds numbers and remains unsteady through the trachea exit. Regions of flow separation that develop due to adverse pressure gradients in rapidly expanding regions following geometric constrictions produce this unsteadiness. Although our simulations correspond to steady inspiration, the timescales associated with the dynamics of turbulent fluctuations are much faster than a typical

inhalation maneuver and therefore should play a significant role in the development of unsteadiness in cyclic breathing. Particle deposition fractions increase with particle size and inhalation flow rate. Deposition fractions and locations differ significantly between the three models. In particular, flow and particle deposition in the larynx and trachea are shown to be sensitive to differences in the anatomy of the pharynx/larynx double constriction feature, suggesting that patient-specific deposition predictions may be required for accurate modeling. DF is significant in the nasal passages and larynx/trachea regions of the airway at most flow rates, and both must be included in CFD simulations for accurate predictions of particle penetration into the bronchial tree. The computed and experimental data may be used to inform algebraic models of particles entering the primary bronchi.

ACKNOWLEDGMENTS

The authors acknowledge Dr. Jerold R. Bottiger at the Edgewood Chemical Biological Center for assisting with the experiments, Dr. Paul A. Dabisch and Matthew G. Lackemeyer at the National Biodefense Analysis and Countermeasures Center for providing the CT scans, and Ryan Gilley for segmenting and fabricating the airway models. They also acknowledge the contributions of Dr. Beth L. Laube at the Johns Hopkins University School of Medicine through many useful discussions. This work was supported by the U.S. Army High Performance Computing Research Center (AHPCRC). Computer simulations were performed on the U.S. Air Force's Lightning cluster.

[1] T. B. Martonen, I. M. Katz, and C. J. Musante, A nonhuman primate aerosol deposition model for toxicological and pharmaceutical studies, Inhal. Toxicol. **13**, 307 (2001).

[2] J. D. Schroeter, B. Asgharian, O. T. Price, and G. E. McClellan, Computational fluid dynamics simulations of inhaled nano- and microparticle deposition in the rhesus monkey nasal passages, Inhal. Toxicol. **25**, 691 (2013).

[3] D. Smith, P. Trennery, D. Farningham, and J. Klapwijk, The selection of marmoset monkeys (Callithrix jacchus) in pharmaceutical toxicology, Lab. Anim. **35**, 117 (2001).

[4] P. A. Dabisch, Z. Xu, J. A. Boydston, J. Solomon, J. K. Bohannon, J. J. Yeager, J. R. Taylor, R. J. Reeder, P. Sayre, J. Seidel, D. J. Mollura, M. C. Hevey, P. B. Jahrling, and M. G. Lackemeyer, Quantification of regional aerosol deposition patterns as a function of aerodynamic particle size in rhesus macaques using PET/CT imaging, Inhal. Toxicol. **29**, 506 (2017).

[5] J. M. DeSesso, The relevance to humans of animal models for inhalation studies of cancer in the nose and upper airways, Qual. Assur. **2**, 213 (1993).

[6] J. R. Harkema, Comparative aspects of nasal airway anatomy: Relevance to inhalation toxicology, Toxicol. Pathol. **19**, 321 (1991).

[7] D. R. Klonne, C. E. Ulrich, M. G. Riley, T. E. Hamm, K. T. Morgan, and C. S. Barrow, One-year inhalation toxicity study of chlorine in rhesus monkeys (Macaca mulatta), Fundam. Appl. Toxicol. **9**, 557 (1987).

[8] S. A. Carey, K. R. Minard, L. L. Trease, J. G. Wagner, G. J. M. Garcia, C. A. Ballinger, J. S. Kimbell, C. G. Plopper, R. A. Corley, E. M. Postlethwait, and J. R. Harkema, Three-dimensional mapping of ozone-induced injury in the nasal airways of monkeys using magnetic resonance imaging and morphometric techniques, Toxicol. Pathol. **35**, 27 (2007).

[9] T. M. Monticello, K. T. Morgan, J. I. Everitt, and J. A. Popp, Effects of formaldehyde gas on the respiratory tract of rhesus monkeys. Pathology and cell proliferation, Am. J. Pathol. **134**, 515 (1989).

[10] K. J. Nikula, K. J. Avila, W. C. Griffith, and J. L. Mauderly, Lung tissue responses and sites of particle retention differ between rats and cynomolgus monkeys exposed chronically to diesel exhaust and coal dust, Toxicol. Sci. **37**, 37 (1997).

[11] D. C. Dorman, M. F. Struve, B. A. Wong, J. A. Dye, and I. D. Robertson, Correlation of brain magnetic resonance imaging changes with pallidal manganese concentrations in rhesus monkeys following subchronic manganese inhalation, Toxicol. Sci. **92**, 219 (2006).

[12] T. B. Griffin, F. Coulston, H. Wills, and J. C. Russell, Biologic effects of airborne particulate lead on continuously exposed rats and rhesus monkeys, Environmental Quality and Safety, Supplement **2**, 202 (1975).
[13] H. A. Druett, D. W. Henderson, L. Packman, and S. Peacock, Studies on respiratory infection: I. The influence of particle size on respiratory infection with anthrax spores, Epidemiol. Infect. **51**, 359 (1953).
[14] W. C. Day and R. F. Berendt, Experimental tularemia in Macaca mulatta: Relationship of aerosol particle size to the infectivity of airborne Pasteurella tularensis, Infect. Immun. **5**, 77 (1972).
[15] J. T. Kelly, B. Asgharian, and B. A. Wong, Inertial particle deposition in a monkey nasal mold compared with that in human nasal replicas, Inhal. Toxicol. **17**, 823 (2005).
[16] H. C. Yeh, Y. S. Cheng, Y. F. Su, and K. T. Morgan, Deposition of radon progeny in nonhuman primate nasal airways, in *Indoor Radon and Lung Cancer: Reality or Myth?* (Battelle Press, Richland, WA, 1992).
[17] H.-C. Yeh, B. A. Muggenburg, and J. R. Harkema, *In vivo* deposition of inhaled ultrafine particles in the respiratory tract of rhesus monkeys, Aerosol Sci. Technol. **27**, 465 (1997).
[18] J. B. Grotberg, Pulmonary flow and transport phenomena, Annu. Rev. Fluid Mech. **26**, 529 (1994).
[19] J. B. Grotberg, Respiratory fluid mechanics and transport processes, Annu. Rev. Biomed. Eng. **3**, 421 (2001).
[20] C. D. Bertram and D. P. Gaver, Biofluid mechanics of the pulmonary system, Ann. Biomed. Eng. **33**, 1681 (2005).
[21] C. Kleinstreuer and Z. Zhang, Airflow and particle transport in the human respiratory system, Annu. Rev. Fluid Mech. **42**, 301 (2010).
[22] W. Hofmann, Modelling inhaled particle deposition in the human lung—A review, J. Aerosol Sci. **42**, 693 (2011).
[23] P. W. Longest and L. T. Holbrook, *In silico* models of aerosol delivery to the respiratory tract—Development and applications, Adv. Drug Delivery Rev. **64**, 296 (2012).
[24] C.-L. Lin, M. H. Tawhai, and E. A. Hoffman, Multiscale image-based modeling and simulation of gas flow and particle transport in the human lungs: Gas flow and particle transport in the human lungs, Wiley Interdisc. Rev.: Syst. Biol. Med. **5**, 643 (2013).
[25] G. M. Kepler, R. B. Richardson, K. T. Morgan, and J. S. Kimbell, Computer simulation of inspiratory nasal airflow and inhaled gas uptake in a Rhesus Monkey, Toxicol. Appl. Pharmacol. **150**, 1 (1998).
[26] J. Xi and P. W. Longest, Transport and deposition of micro-aerosols in realistic and simplified models of the oral airway, Ann. Biomed. Eng. **35**, 560 (2007).
[27] C.-L. Lin, M. H. Tawhai, G. McLennan, and E. A. Hoffman, Characteristics of the turbulent laryngeal jet and its effect on airflow in the human intra-thoracic airways, Respir. Physiol. Neurobiol. **157**, 295 (2007).
[28] J. Choi, M. H. Tawhai, E. A. Hoffman, and C.-L. Lin, On intra- and intersubject variabilities of airflow in the human lungs, Phys. Fluids **21**, 101901 (2009).
[29] A. R. Lambert, P. T. O'shaughnessy, M. H. Tawhai, E. A. Hoffman, and C.-L. Lin, Regional deposition of particles in an image-based airway model: Large-eddy simulation and left-right lung ventilation asymmetry, Aerosol Sci. Technol. **45**, 11 (2011).
[30] Z. Zhang, C. Kleinstreuer, and S. Hyun, Size-change and deposition of conventional and composite cigarette smoke particles during inhalation in a subject-specific airway model, J. Aerosol Sci. **46**, 34 (2012).
[31] Z. Zhang, C. Kleinstreuer, and Y. Feng, Vapor deposition during cigarette smoke inhalation in a subject-specific human airway model, J. Aerosol Sci. **53**, 40 (2012).
[32] Z. Zhang and C. Kleinstreuer, Transient airflow structures and particle transport in a sequentially branching lung airway model, Phys. Fluids **14**, 862 (2002).
[33] Z. Zhang and C. Kleinstreuer, Airflow structures and nano-particle deposition in a human upper airway model, J. Comput. Phys. **198**, 178 (2004).
[34] J. Xi, P. W. Longest, and T. B. Martonen, Effects of the laryngeal jet on nano- and microparticle transport and deposition in an approximate model of the upper tracheobronchial airways, J. Appl. Physiol. **104**, 1761 (2008).
[35] J. A. Bernate, T. S. Geisler, S. Padhy, E. S. G. Shaqfeh, and G. Iaccarino, Study of the flow unsteadiness in the human airway using large eddy simulation, Phys. Rev. Fluids **2**, 083101 (2017).

[36] B. Asgharian, O. Price, G. McClellan, R. Corley, D. R. Einstein, R. E. Jacob, J. Harkema, S. A. Carey, E. Schelegle, D. Hyde, J. S. Kimbell, and F. J. Miller, Development of a rhesus monkey lung geometry model and application to particle deposition in comparison to humans, Inhal. Toxicol. **24**, 869 (2012).

[37] F. Ham and G. Iaccarino, Energy conservation in collocated discretization schemes on unstructured meshes, in *CTR Annual Research Briefs* (Center for Turbulence Research, Stanford, 2004), pp. 3–14.

[38] F. Ham, K. Mattsson, G. Iaccarino, and P. Moin, Towards time-stable and accurate LES on unstructured grids, in *Complex Effects in Large Eddy Simulations* (Springer, Berlin/Heidelberg, 2007), pp. 235–249.

[39] P. A. Davidson, *Turbulence: An Introduction for Scientists and Engineers* (Oxford University Press, Oxford, UK, 2004).

[40] M. Germano, U. Piomelli, P. Moin, and W. H. Cabot, A dynamic subgrid-scale eddy viscosity model, Phys. Fluids A **3**, 1760 (1991).

[41] J. K. Comer, C. Kleinstreuer, and C. S. Kim, Flow structures and particle deposition patterns in double-bifurcation airway models. Part 2. Aerosol transport and deposition, J. Fluid Mech. **435**, 55 (2001).

[42] Y. Wang and S. Elghobashi, On locating the obstruction in the upper airway via numerical simulation, Respir. Physiol. Neurobiol. **193**, 1 (2014).